Nano Energy 47 (2018) 547–555

Contents lists available at ScienceDirect

Nano Energy

journal homepage: www.elsevier.com/locate/nanoen

Full paper

One-step production of O-N-S co-doped three-dimensional hierarchical porous carbons for high-performance supercapacitors

Gongyuan Zhao[a,c], Chong Chen[a], Dengfeng Yu[b], Lei Sun[a], Chenhui Yang[a], Hong Zhang[b], Ye Sun[b,*], Flemming Besenbacher[c,*], Miao Yu[a,*]

[a] State Key Laboratory of Urban Water Resource and Environment, School of Chemistry and Chemical Engineering, Harbin Institute of Technology, Harbin 150001, China
[b] Condensed Matter Science and Technology Institute and Department of Physics, School of Science, Harbin Institute of Technology, Harbin 150080, China
[c] Interdisciplinary Nanoscience Center (iNANO) and Department of Physics and Astronomy, Aarhus University, Aarhus 8000, Denmark

ARTICLE INFO

Keywords:
Hierarchical porous carbon
Co-doping
Supercapacitor
Biomass
High energy density

ABSTRACT

Besides the complex and low-yield synthesis, attaining high energy density whilst maintaining high power density remains as the major challenge for supercapacitor applications. Herein, we report one-step production of O-N-S co-doped hierarchical porous carbons (HPCs) from ant powder. The resultant product possesses a large specific surface area (2650 $m^2 g^{-1}$), a typical three-dimensional (3-D) framework comprised of interconnected macro-, meso- and micropores with suitable pore size distribution, together with an appropriate heteroatom doping of O, N, and S. These distinct features have afforded an ultra-high specific capacitance of 576 $F g^{-1}$ at a current density of 1.0 $A g^{-1}$ in a three-electrode system and 352 $F g^{-1}$ at a current density of 0.1 $A g^{-1}$ in a two-electrode system, using 6 mol L^{-1} KOH aqueous as electrolyte. Moreover, the high rate retention of ~80% from 1.0 $A g^{-1}$ to 10.0 $A g^{-1}$ and the high cycling stability (~ 5% loss over 10,000 cycles) have been also demonstrated. Most importantly, the fabricated symmetric supercapacitors using 1-ethyl-3-methylimidazolium tetrafluoroborate ($EMIMBF_4$) electrolyte delivered an energy density as high as 107 Wh kg^{-1} at a power density of 900 W kg^{-1}, and a remarkable energy density of 67 Wh kg^{-1} can be retained even at a power density as high as 18,000 W kg^{-1}. These values represent a new performance record for supercapacitors based on biomass-derived carbons, indicating the great promise of these HPCs for high-performance electrochemical energy storage.

1. Introduction

Focusing on the global challenges of energy and pollution caused by the severe consumption of fossil fuels, high-performance energy storage devices based on renewable materials are intensively demanded [1–5]. As the most promising devices for this purpose, supercapacitors have attracted tremendous attention due to their rapid charge–discharge rate, excellent cycling stability, and high power density, superior to lithium-ion batteries [6–8]. However, the difficulties in attaining high energy density whilst maintaining high power density have severely hindered the application of supercapacitors.

To enhance the electrochemical performance of supercapacitors, enormous effort has been devoted to produce carbon-based electrode materials simultaneously possessing the following features: (1) high specific surface area (SSA) to provide a large number of active sites that can accommodate charge [9,10]; (2) interconnected hierarchical micro-, meso- and macro-pores that are able to facilitate fast ion diffusion into internal pores under high charge–discharge conditions [11,12]; (3) three-dimensional (3-D) frameworks that enhance mechanical stability and further benefit the rapid ion transfer [13,14]; (4) doping with heteroatoms (*e.g.* O, N, or S) that promote the wettability and pseudo-capacitance properties [15–17]. However, to produce carbon materials with abovementioned hierarchical structure, certain hard templates (*e.g.,* MgO, ZnO, SiO_2) and sophisticated post-synthetic procedures are often required [18–22]. And to realize heteroatom doping, chemical reagents (*e.g.,* ammonia gas, urea, melamine, sulfourea) and even processes employing hazardous chemical reactions are mandatory [23–26]. Consequently, the complex, time-consuming and low-yield synthesis has largely limited the application potentials. Therefore, it would be highly desirable to produce high-performance HPCs from renewable feedstocks using simple and efficient methods.

Inspiringly, the use of biomass as a carbon precursor has quickly emerged to be a popular alternative route for the production of HPCs [27–30]. Besides the sustainability and eco-friendliness of biomass, their intrinsic composition and natural structural features have afforded them considerable potential as the precursors for carbon materials used

* Corresponding authors.
E-mail addresses: sunye@hit.edu.cn (Y. Sun), fbe@inano.au.dk (F. Besenbacher), miaoyu_che@hit.edu.cn (M. Yu).

https://doi.org/10.1016/j.nanoen.2018.03.016
Received 7 January 2018; Received in revised form 5 March 2018; Accepted 5 March 2018
Available online 07 March 2018

in supercapacitors. For example, activated carbons derived from carbonization and KOH treatment of human hair were shown to have a specific capacitance of 382 F g^{-1} at current density of 0.5 A g^{-1} in a three-electrode system, using 6 mol L^{-1} KOH aqueous electrolyte [27]. N-P-O co-doped 3-D graphene produced by red phosphorous-assisted "cutting-thin biomass" technique presented a SSA of 1406 $m^2 \cdot g^{-1}$ and a high specific capacitance of 426 F g^{-1} at 0.5 A g^{-1} in a three-electrode system [28]. Recently, Gao et al. reported nitrogen-doping hierarchical porous carbons using poplar catkins as the precursor, which gave a high SSA of 1462 m^2 g^{-1} and a specific capacitance of 251 F g^{-1} at 0.5 A g^{-1}, using 1 mol L^{-1} H_2SO_4 aqueous electrolyte [29]. In our earlier work, we have reported supercapacitors containing 3-D porous carbon nanosheets derived from plant epidermis that are rich in cellulose, protein, and other carbohydrates. The tough and pliable epidermis structure functioned as an effective skeleton for the formation of 3-D frameworks in the carbonization process, resulting in specific capacitances as high as 470 F g^{-1} and 310 F g^{-1} at 1.0 A g^{-1} in three- and two-electrode system using 6 mol L^{-1} KOH electrolyte. These carbons demonstrated a high energy density of 54 Wh kg^{-1} at a power density of 375 W kg^{-1}, when 1-ethyl-3-methylimidazolium tetrafluoroborate ($EMIMBF_4$) was used as electrolyte [30]. Albeit all the progress, biomass-derived porous carbons which are capable to generate supercapacitors with even greater energy density and specific capacitance remain highly desirable.

Insects are highly diverse and widely distributed throughout the planet. Interestingly, the distinct natural features of certain insects could be favorable for the production of HPCs: (1) exoskeleton composed of chitin, an oligosaccharide biopolymer that could potentially be an ideal candidate for the formation of robust 3-D scaffolding frameworks in the carbonation process; (2) composition rich in calcium, iron, magnesium, manganese and zinc salts and a high content of protein, which could potentially function as natural hard templates to generate hierarchical porous structures, and simultaneously afford a range of co-doping with N, O, S, and P. Although a huge variety of biomass have been applied for HPCs production, the potential of insect materials remains unexplored. Commercially available for pharmaceutical purposes, the low-cost ant powder (powder of dried dead ants) has enabled the possibility.

In this work, we have produced 3-D scaffolding frameworks of O-N-S co-doped HPCs from ant powder for high-performance supercapacitor applications, using one-step simultaneous carbonization and activation (Scheme 1). The resultant HPCs showed a remarkably high SSA of 2650 m^2 g^{-1}, with a defined hierarchical porous structure and appropriate pore-size distribution. These physical properties enabled an ultra-high specific capacitance of 576 F g^{-1} at a current density of 1.0 A g^{-1} in a three-electrode system using 6 mol L^{-1} KOH aqueous electrolyte. Moreover, the high rate retention of ~ 80% from 1.0 A g^{-1} to 10.0 A g^{-1} and the high cycling stability (~ 5% loss over 10,000 cycles) further illustrated the superiorities of the product. Importantly, the fabricated symmetric supercapacitors using the ionic liquid $EMIMBF_4$ electrolyte delivered an energy density as high as 107 Wh kg^{-1} at a power density of 900 W kg^{-1}, and 67 Wh kg^{-1} at 18,000 W kg^{-1}. These values represent a new performance record for supercapacitors based on biomass-derived carbons.

2. Experimental section

2.1. Synthesis of HPCs from ant powder

The ant powder (Lan Xin, China) was washed using distilled water and ethanol, and dried at 70 °C for 12 h. In a typical procedure, 2.0 g of ant powder and 2.0 g of KOH were mixed together in a mortar, and the mixture was then transferred into a porcelain boat located in a tube furnace for carbonization at 800 °C for 2 h under an Ar atmosphere. The obtained powder was washed with dilute HCl solution (10%) and distilled water, and then dried at 100 °C for 12 h to afford an ant-derived sample that was classified as '*AHPC*'. Ant powder carbonized at 800 °C under Ar for 2 h in the absence of KOH was classified as '*Control*'.

2.2. Material characterization

Microstructures, morphologies and crystallinity of the samples were characterized using field-emission scanning electron microscopy (FESEM, FEI, Quanta 200F equipped with an energy dispersive X-ray (EDX) spectrometer), transmission electron microscopy (TEM, FEI, Tecnai-G2-F30), X-ray diffraction (XRD, PANalytical, X'Pert Pro, using Cu Kα radiation), Raman spectrometry (Renishaw, inVia, under excitation at 532 nm), and X-ray photoelectron spectroscopy (XPS, Thermo Fisher Scientific, ESCALAB250Xi, using Al kα monochromatic X-ray source). SSA values of the samples that had been vacuum-dried at 200 °C for 30 h were calculated using the multi-point Brunauer-Emmett-Teller (BET) method, with pore size distribution calculated using density functional theory modeling of nitrogen adsorption-desorption isotherms carried out at 77.4 K (Quantachrome, Autosorb-iQ). Thermogravimetric analysis of the ant powder was performed using a Netzsch STA analyzer at a heating rate of 10 °C min^{-1}.

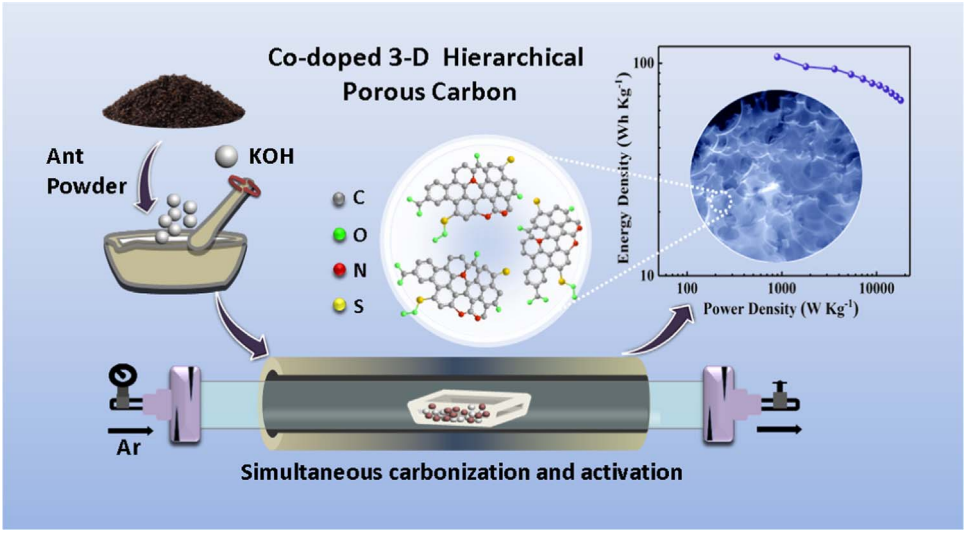

Scheme 1. Schematic illustration of the production processes for the 3-D hierarchical porous carbons.

2.3. Electrochemical measurements

The electrochemical properties of the carbon products were first explored using a three-electrode system in 6 mol L^{-1} KOH aqueous solution. Carbon materials, acetylene black and polytetrafluoroethylene binder were mixed together to give a weight ratio of 80:15:5 in ethanol and form slurry that was pressed onto a nickel foam current collector (1 × 1 cm^2). The electrode materials were then dried at 100 °C for 12 h to afford working electrodes, with the mass loading of the active materials in each working electrode determined as ~ 3.0 mg cm^{-2}. A platinum foil electrode (2 × 2 cm^2) and an Hg/HgO electrode were used as the counter electrode and reference electrode in a standard three-electrode setup, respectively. Cyclic voltammetry (CV), galvanostatic charge–discharge (GCD) and electrochemical impedance spectroscopy (EIS) were used to study the capacitive performance of the samples. Symmetrical two-electrode supercapacitors were assembled in a 2032 stainless steel coin cell using glassy paper as a membrane to separate the two working electrodes containing mass loadings of ~ 3.0 mg cm^{-2} on each working electrode. 6 mol L^{-1} KOH, 1 mol L^{-1} Na_2SO_4, and EMIM-BF_4 were employed as electrolytes, with the operating voltages for GCD and CV measurements set as 0 − 1.0 V, 0 − 1.6 V and 0 − 3.6 V, respectively. The calculation details of the specific capacitance, specific energy density and specific power density are described in the Supporting information (SI).

3. Results and discussion

3.1. Material characteristics

The morphologies of the carbon products were first characterized using SEM. As shown in Fig. 1a, the '*Control*' sample was consisted of plate-like structures with diameters of tens of microns and a thickness ranging from hundreds of nanometers to several microns. These plate-like structures presented relatively smooth surfaces with no apparent pores, and such morphology was further ascertained using TEM imaging (Fig. 1b). Treated with KOH, the samples were modified significantly. As well-demonstrated in the literature [31], KOH can play vital roles in carbon activation during the pyrolysis, and react with carbon following $6KOH + 2C \rightarrow 2K + 3H_2 + 2K_2CO_3$ to generate porous structures in carbon materials with the aid of HCl washing. Consistently, SEM (Fig. 1c − 1d) and TEM (Fig. 1e) images of the '*AHPC*' revealed 3-D scaffolding frameworks of porous carbon nanosheets. The high-density micron-sized pores and open cavities of the '*AHPC*' are apparently favorable for the quick transportation of electrolyte ions. Promisingly, the high-resolution TEM image shown in Fig. 1f clearly revealed the existence of plentiful micropores in the '*AHPC*'.

The pore properties of the carbon products were then examined using nitrogen adsorption and desorption measurements. The nitrogen adsorption-desorption isotherm and pore size distribution curve of the '*Control*' were shown in Fig. 2a − 2b, respectively. A small SSA of 125 $m^2 \cdot g^{-1}$, a small pore volume of 0.1 cm^3 g^{-1}, and an average pore width (APW) of 3.8 nm can be deduced. In contrast to the undeveloped pore structures of the '*Control*', the '*AHPC*' was confirmed to contain well-developed pore structures with a significant SSA of 2650 m^2 g^{-1}, a very large pore volume of 1.4 cm^3 g^{-1} (micropore volume of 0.9 cm^3 g^{-1}), and an APW of 2.1 nm. The results are consistent with the SEM and TEM images shown in Fig. 1c–1f. The nitrogen adsorption-desorption isotherm of the '*AHPC*' (Fig. 2c) gave a combined Type I and IV isotherm with a hysteresis loop. The dramatic increase in the isotherm at a relatively low pressure ($P/P_0 < 0.2$) can be attributed to the presence of high-density micropores. The hysteresis loop from a capillary condensation process at medium relative pressure ($P/P_0 = 0.4 - 0.8$) demonstrates the presence of mesopores. Furthermore, the slight rise at high relative pressure ($P/P_0 = 0.9 - 1.0$) reveals the presence of macropores. The '*AHPC*' can be therefore concluded to be hierarchical porous carbon. Furthermore, the pore size distribution of the '*AHPC*' reveals micropores with dimensions of 0.6, 0.9, 1.2 and 2.0 nm, together with mesopores of 2.0–6.0 nm (Fig. 2d). Accumulation of charge or electrolyte ions occurs primarily at micropores, and macropores and mesopores are known to be capable of transferring electrolytes to micropores and improve the efficiency of the conduction process [32–34]. The hierarchical '*AHPC*' containing abundant micropores, mesopores and macropores has, therefore, excellent potential as an electrode material for supercapacitor applications.

The crystallinity and composition of carbon materials are also critical for their ability to function as a supercapacitor. The XRD patterns of the '*Control*' and '*AHPC*' are presented in Fig. 2e, where the observed peak centered at ~23° can be assigned to the (002) plane spacing corresponding to the interlayer spacing of the graphite carbon, and the peak centered at ~43° can be attributed to the in-plane (100) spacing of

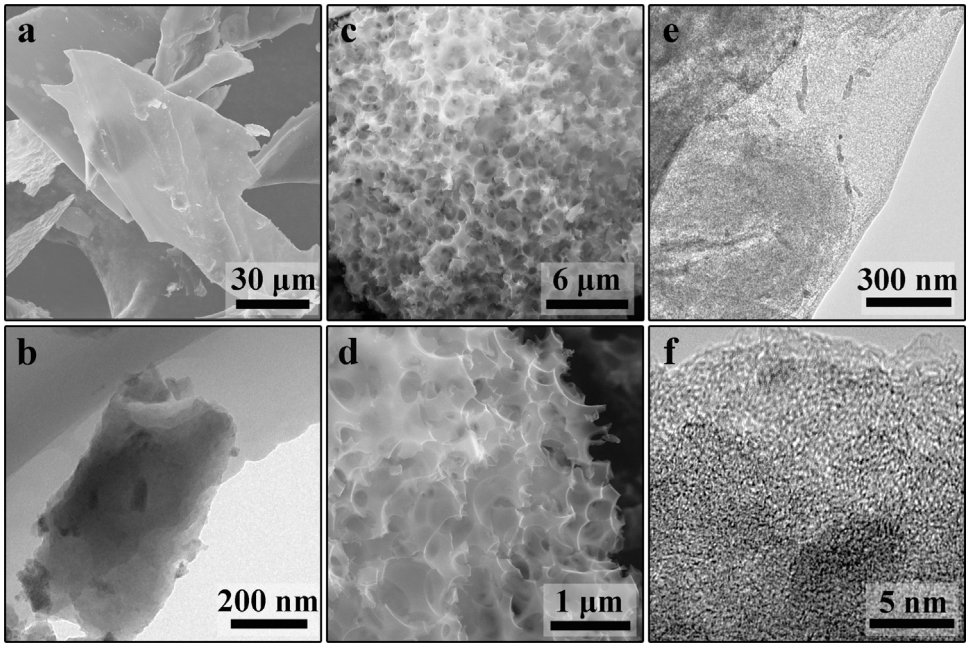

Fig. 1. (a) SEM and (b) TEM images of the '*Control*'. (c, d) SEM and (e, f) TEM images of the '*AHPC*'.

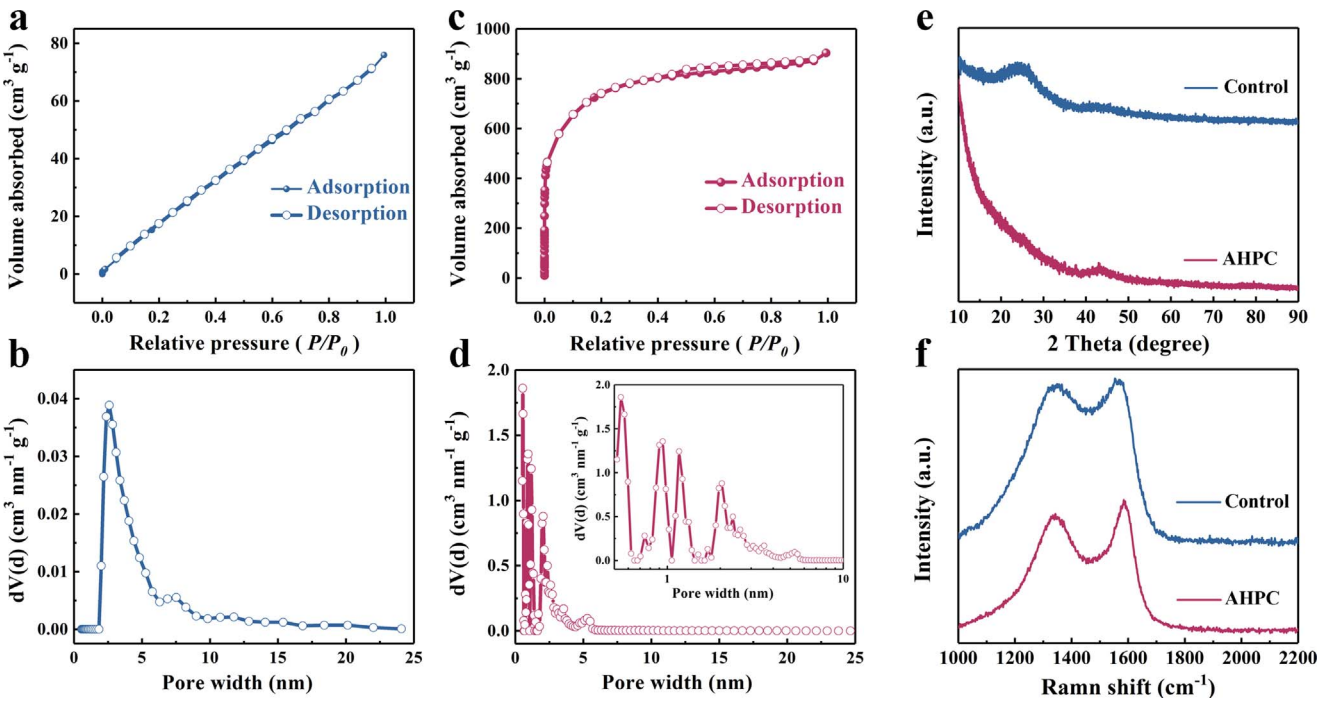

Fig. 2. Nitrogen adsorption-desorption isotherms and pore size distributions of (a, b) the *'Control'*, and (c, d) *'AHPC'* sample. (e) XRD patterns and (f) Raman spectra of the*'Control'* and *'AHPC'* sample.

the graphite carbon. These patterns indicate that both samples were formed by turbostratic carbon. Moreover, it is noticed that the pattern of the '*AHPC*' presented a significantly enhanced intensity in its small-angle region ($2\theta < 20^{\circ}$), indicating the presence of high-density micropores, thus confirming the results of the TEM studies and the nitrogen adsorption-desorption isotherm analysis. Additionally, Raman spectroscopy was also employed to investigate the crystallinity of the samples. As shown in Fig. 2f, a G band located at ~ 1580 cm^{-1} (characteristic feature of graphitic layers) and a D band located at ~ 1350 cm^{-1} (characteristic of disordered carbon or defective graphitic structures) were identified in the Raman spectra of both samples, consistent with the results in the literature [35]. The intensity ratio of the G to D bands (I_G/I_D) can be used to evaluate the degree of graphitization. Given the I_G/I_D = 1.03 and 1.12 for the '*Control*' and '*AHPC*', respectively, the '*AHPC*' possessed a slightly higher degree of graphitization, likely due to the reduced amount of heterotoms upon KOH treatment, which is consistent with the stronger in-plane (101) peak presented in the XRD pattern of the '*AHPC*' sample (Fig. 2e).

The chemical composition of the '*AHPC*' sample was further characterized by XPS (Fig. S1), which revealed the presence of C (~ 93.0 at %), O (~ 5.0 at%), N (~ 1.5 at%), and S (~ 0.5 at%). The high-resolution C 1 s spectrum (Fig. 3a) of the '*AHPC*' was resolved into five individual peaks, corresponding to C-S (~ 283.8 eV), C-C (~ 284.8 eV), C-N (~ 285.7 eV), C=O (~ 287.1 eV), and COOR (~ 290.0 eV) binding [36,37]. The high-resolution O 1 s spectrum (Fig. 3b) revealed the presence of three oxygen-based components, including C=O (~ 532.2 eV), C-O (~ 533.2 eV), and COOR (534.0 eV) [38]. The N 1 s spectrum (Fig. 3c) was deconvoluted into two peaks located at ~ 399.7 and ~ 401.0 eV, corresponding to pyridine (N-5) and quaternary (N-4) nitrogen groups, respectively [39]. The S 2p spectrum (Fig. 3d) indicated the presence of three deconvoluted peaks, where the two centered at ~ 164.3 eV and ~ 165.5 eV attributable to C-S bonding and one centered at 168.8 eV assigned to an oxidized sulfur moiety (-SO_n-) [26,40]. It has been well-addressed that the doping of O, N and S heteroatoms and the associated functional groups can enhance the wettability of electrode materials, leading to significant increases in the accessible surface area for electrolyte. We can then conclude that the '*AHPC*' possesses a well-developed hierarchical porous structure with a large SSA, a high degree of graphitization and a favorable doping of heteroatoms. These properties may have endowed the product significant potential as a high-performance electrode material for supercapacitors and other energy conversion and storage devices.

3.2. Electrochemical properties in a three-electrode system

A pair of reference samples were produced *via* pretreatment of 2.0 g ant power respectively with 1.0 g and 3.0 g KOH, to afford materials that were classified as '*AHPC-a*' and '*AHPC-b*'. The electrochemical properties of the four HPC samples were measured using a three-electrode system using 6 mol L^{-1} KOH aqueous as electrolyte. CV curves measured in a potential window of 0–1 V at a scan rate of 100 mV s^{-1} and GCD plots at a current density of 1 A g^{-1} are presented in Fig. S2. The '*AHPC*' electrode produced the best electrochemical performance among the four samples, exhibiting CV curves with the largest area and most rectangular shape, as well as the longest charge – discharge time and the lowest IR drop in its GCD plots. The CV curves at different scan rates from 5 to 100 mV s^{-1} and GCD curves at current densities in the range of 1–20 A g^{-1} for the '*AHPC*' are shown in Fig. 4a – 4b, which are characteristic of typical EDLC. In Fig. 4c, we observed small equivalent series resistance in the Nyquist plots of the '*AHPC*', which can benefit high rate capability. Based on the CV and GCD results, an ultra-high specific capacitance of 576 F g^{-1} at 1 A g^{-1} was measured from the '*AHPC*' electrode (Fig. 4d). Moreover, the values of specific capacitance were recorded as high as 300 F g^{-1} and 267 F g^{-1} even at high current densities of 10 A g^{-1} and 20 A g^{-1}, respectively.

3.3. Electrochemical properties in a two-electrode system using aqueous electrolyte

The remarkable performance of the '*AHPC*' in the three-electrode system inspired us to assemble symmetric supercapacitors in alkaline 6 mol L^{-1} KOH and neutral 1 mol L^{-1} Na_2SO_4 solutions to investigate its potential for practical applications. Being neutral, Na_2SO_4 electrolyte can provide a larger voltage window (1.6 V) than acid and alkaline

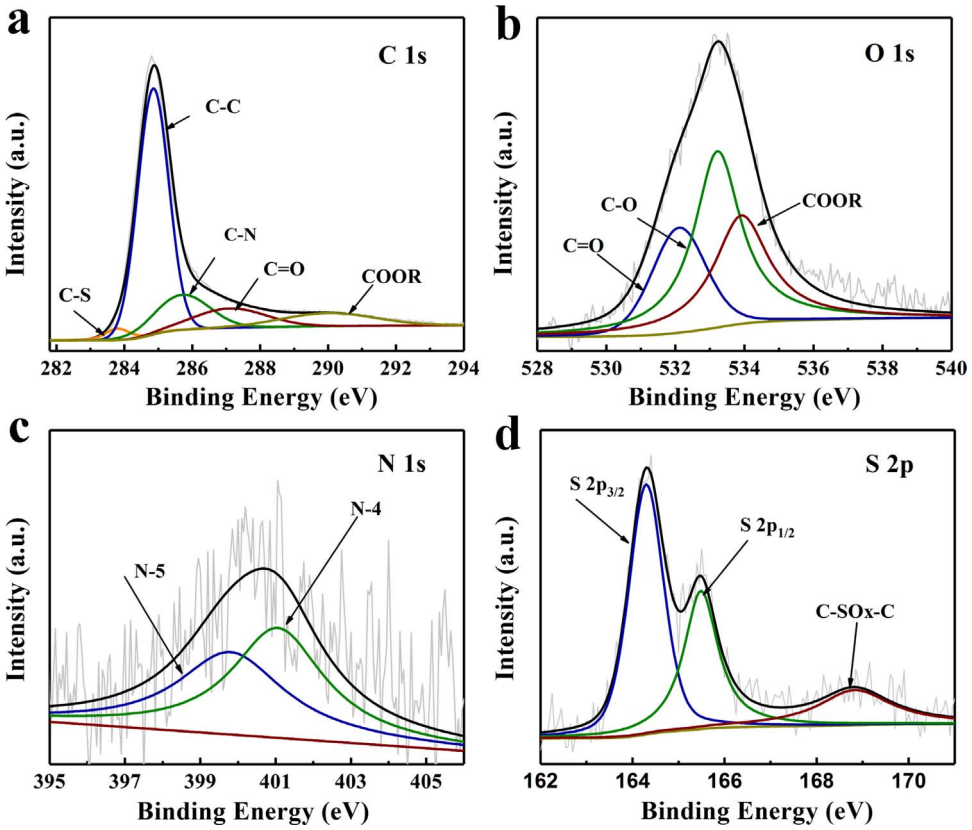

Fig. 3. XPS spectra of (a) C 1s, (b) O 1s, (c) N 1s, (d) S 2p for the '*AHPC*' sample.

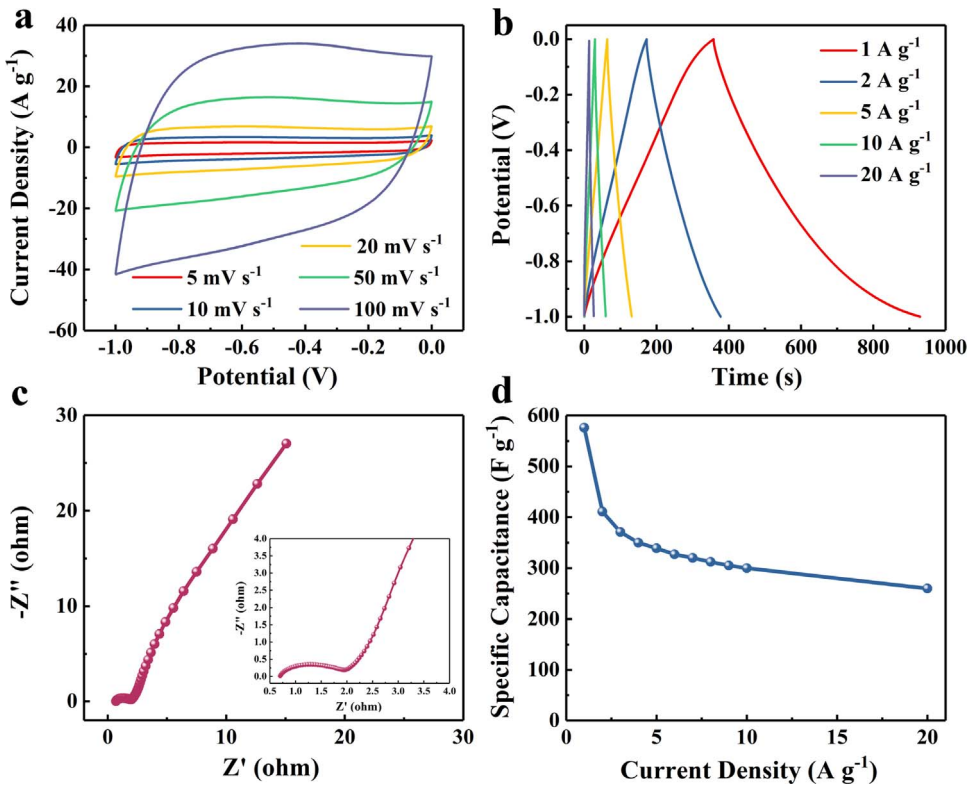

Fig. 4. (a) CV curves at different scan rates from 5 to 100 mV s^{-1}, (b) GCD curves at current densities in the range of 1–20 A g^{-1}, (c) Nyquist plots and (d) gravimetric capacitances at different current densities from 1 to 20 A g^{-1} of the '*AHPC*' sample measured in a three-electrode system using 6 mol L^{-1} KOH as the electrolyte.

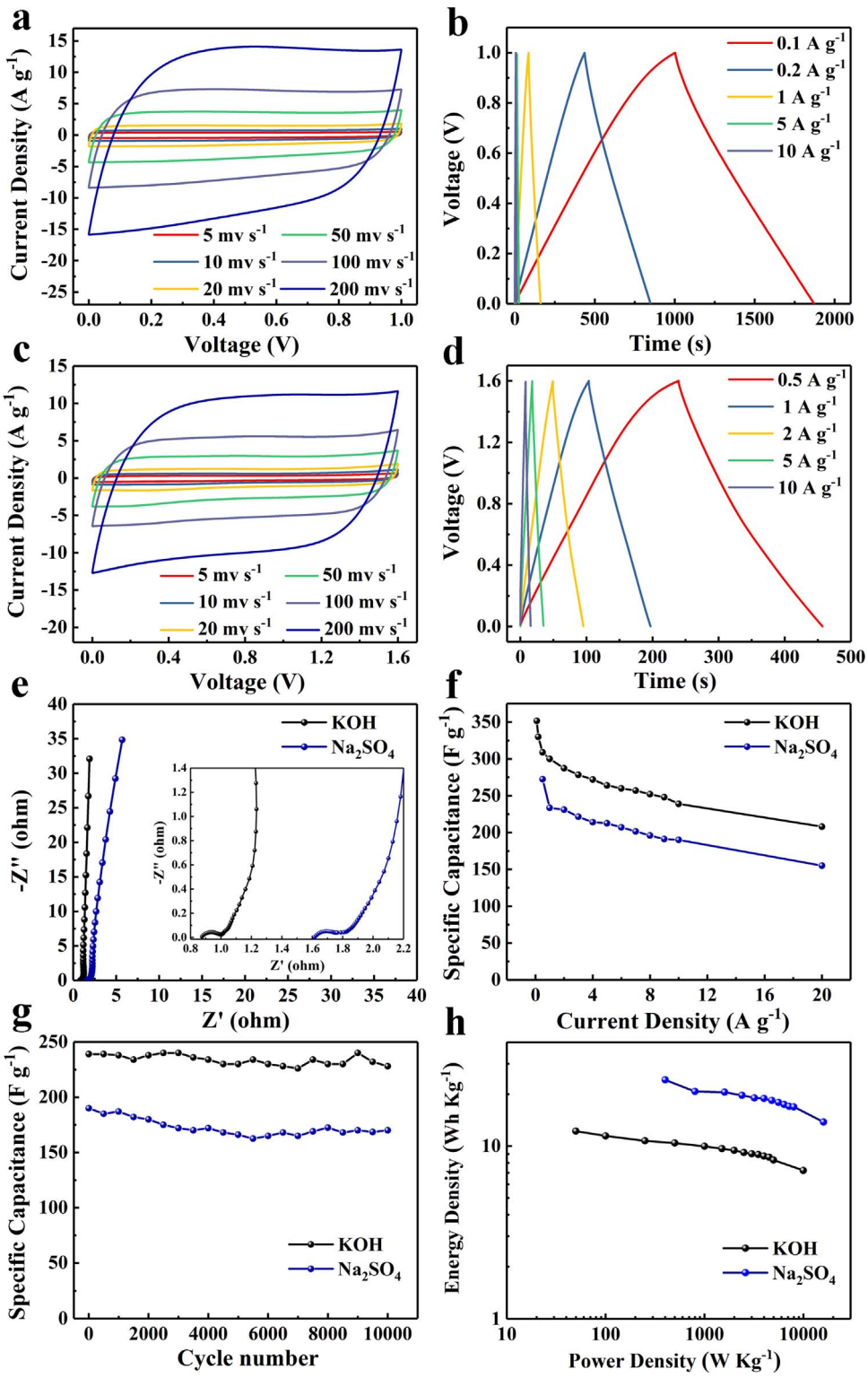

Fig. 5. Electrochemical performance characteristics of the '*AHPC*' measured in a two-electrode system using 6 mol L^{-1} KOH and 1 mol L^{-1} Na_2SO_4 as electrolytes, respectively. (a) CV curves at different scan rates from 5 to 200 mV s^{-1} in a voltage window of 0–1.0 V, and (b) GCD curves at different current densities from 0.1 to 10 A g^{-1} in 6 mol L^{-1} KOH. (c) CV curves at different scan rates from 5 to 200 mV s^{-1} in a voltage window of 0–1.6 V, and (d) GCD curves at different current densities from 0.5 to 10 A g^{-1} in 1 mol L^{-1} Na_2SO_4. (e) Nyquist plots, (f) gravimetric capacitances at different current densities, (g) cycling stability performance at a current density of 10 A·g^{-1}, and (h) Ragone plots in 6 mol L^{-1} KOH and 1 mol L^{-1} Na_2SO_4.

electrolytes, since the equilibrium of H^+ and OH^- in Na_2SO_4 is unfavorable for reaction with electrodes to evolve H_2 or O_2 [41]. Moreover, the strong solvation of both alkali metal cation and sulfate anion of Na_2SO_4 electrolyte can effectively benefit its stability at higher voltages. Quasi-rectangular shape CV curves and nearly isosceles triangle GCD curves were observed from the '*AHPC*' electrode in 6 mol L^{-1} KOH solution at charge voltages of 0–1.0 V (Fig. 5a–5b). Such near-ideal EDLC behavior for the '*AHPC*' electrode was also presented when using Na_2SO_4 electrolyte with a potential window of 0–1.6 V (Fig. 5c–5d). It is noteworthy that small drops in IR were also found in the GCD curves measured in both KOH and Na_2SO_4 solutions, even at a high current density of 10 A g^{-1} (IR drop < 120 mV in KOH solution, IR drop <

Table 1
Electrochemical performance of carbon-based supercapacitors.

Biomass precursor	SSA ($m^2 g^{-1}$)	Test system (electrode) / Electrolyte	Current density (A g^{-1})	Specific capacitance (F g^{-1})	Max Energy density (W h kg^{-1})	Power density (W kg^{-1})	Ref.
Sugar	1005	2E/1 M H_2SO_4	1	250	8.7	500	[14]
Willow catkin	1533	3E/6 M KOH	1	298	–	–	[26]
Human hair	1306	2E/ $LiPF_6$	0.1	126	45.3	150	[27]
Artemia cyst shells	1406	3E/6 M KOH	0.5	426	–	–	[28]
Elm samara	1947	3E/6 M KOH	1	470	–	–	[30]
Silk	2557	2E/1 M H_2SO_4	0.1	264	9.1	50	[31]
Soybean Root	2143	2E/6 M KOH	0.5	276	9.6	250	[33]
Tofu	1202	3E/6 M KOH	1	418	–	–	[39]
Corn husk	928	2E/1 M Na_2SO_4	1	187	21.0	875	[42]
Fungus	1103	3E/6 M KOH	0.5	374	–	–	[43]
Sweet potato vines	884	3E/6 M KOH	1	265	–	–	[44]
Nelumbo nucifera	1610	2E/6 M KOH	1	174	6.0	500	[45]
Moringa oleifera	2312	2E/6 M KOH	0.2	181	6.3	102	[46]
Pomelo mesocarps	974	2E/1 M Na_2SO_4	0.1	131	14.7	90	[47]
Seaweeds	746	2E/TEA BF_4	1	94	17.3	1150	[48]
Crab shell	1141	2E/EMIM TFSI	1	113	48.1	1750	[49]
Tobacco rods	2097	2E/ $CH_3(C_2H_5)_3N$ BF_4	0.5	144	31.3	625	[50]
Coconut shell	1874	2E/Et_4N BF_4	1	196	61.2	1500	[51]
Onion husks	2571	2E/TEA BF_4	0.5	188	47.5	675	[52]
Ant powder	2650	3E/6 M KOH	1	576	–	–	This work
		2E/6 M KOH	0.1	352	12.2	50	
		2E/1 M Na_2SO_4	0.5	273	24.2	400	
		2E/ EMIM BF_4	0.5	238	107.1	900	

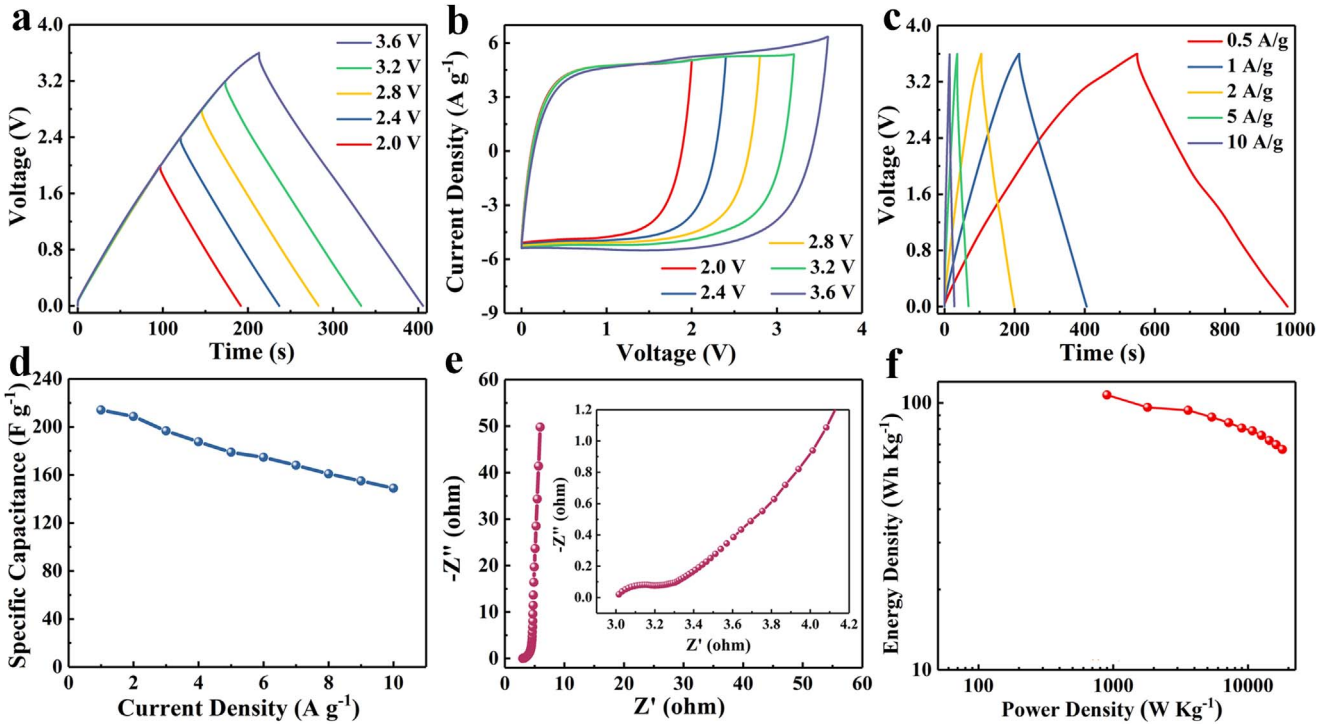

Fig. 6. Electrochemical performance characteristics of the '*AHPC*' electrode measured in a symmetrical supercapacitor using $EMIMBF_4$ as an electrolyte. (a) GCD profiles at 1 A g^{-1}, and (b) CV profiles at 100 mV s^{-1} of the '*AHPC*' electrode at different operation voltages. (c) GCD curves at different current densities from 1 to 20 A g^{-1}, (d) Gravimetric capacitances at different current densities, (e) Nyquist plots under the influence of an amplitude of 5 mV, and (f) Ragone plot of the '*AHPC*' electrode.

180 mV in Na_2SO_4 solution). These phenomena suggest that these supercapacitors have small internal resistances. Their capacitive performance was further confirmed by EIS measurements using an AC voltage amplitude of 5 mV. As shown in Fig. 5e, the Nyquist plots of the supercapacitors using KOH and Na_2SO_4 as electrolytes were both nearly parallel to the imaginary axis (-Z) in the low frequency region, thus providing further evidence of the ideal capacitive performance of the '*AHPC*' electrode. Small values were obtained for the intrinsic ohmic resistance (R_s) (represented by the intercept at the real axis in the high-frequency region), the charge transfer resistance (R_{ct}) (represented by the semicircle shape in medium-frequency region) and the Warburg diffusion resistance (R_w) (represented by the slope of 45° between the semicircle and vertical line). These values all indicate that both supercapacitors have high electrode conductivity levels, good electron transfer rates at the electrode/electrolyte interface, and rapid diffusion of electrolyte ions.

The plots of specific capacitance of the '*AHPC*' electrode at different current densities in the KOH and Na_2SO_4 electrolyte are presented in Fig. 5f. Use of KOH electrolyte gave an ultrahigh specific capacitance of 352 F·g^{-1} at a current density of 0.1 A g^{-1}, together with a retained

capacitance of 225 F g^{-1} at a current density of 20 A g^{-1}. Additionally, a high capacitance retention of 95% was achieved after 10,000 charge–discharge cycles at a current density of 10 A g^{-1} (Fig. 5g), thus indicating the excellent long-term cyclic stability of the '*AHPC*' electrode. The supercapacitor using the Na_2SO_4 electrolyte also demonstrated high performance, producing a high specific capacitance of 273 F g^{-1} at a current density of 0.5 A g^{-1} and a high capacitance retention of 91% at the 10,000th charge–discharge cycles at a current density of 10 A g^{-1}. These results are in good accordance with the Nyquist plots (Fig. S3), where the intrinsic ohmic resistance, the charge transfer resistance, and the length of the Warburg-type lines were only slightly increased after cycling. Promisingly, the maximum energy densities of these supercapacitors were 12 Wh kg^{-1} at a power density of 50 W kg^{-1} using KOH electrolyte and 24 Wh kg^{-1} at a power density of 400 W kg^{-1} in Na_2SO_4 (Fig. 5h), respectively. These values are evidently superior to those of reported carbon-based symmetric supercapacitors in aqueous electrolytes (as summaries in Table 1).

3.4. Electrochemical properties in a two-electrode system using an ionic liquid electrolyte

$EMIMBF_4$ was then used as an ionic liquid electrolyte in an attempt to further increase the performance and energy density of the supercapacitor. GCD measurements at a current density of 1 A g^{-1} and CV measurements at a scan rate of 100 mV s^{-1} were acquired for a supercapacitor using $EMIMBF_4$ electrolyte in a potential range of 2.0–3.6 V. As shown in Fig. 6a−6b, all the CV profiles exhibited rectangular shapes with all the GCD plots displaying perfect linear and symmetrical shapes, indicating good EDLC behavior and high reversibility of this capacitor. The performance was further confirmed from the GCD curves at a current density range of 0.5–10 A g^{-1} using a charge voltage of 3.6 V (Fig. 6c). The calculated specific capacitances of the '*AHPC*' electrode at different current densities are shown in Fig. 6d, achieving a specific capacitance as high as 214 F g^{-1} at 1 A g^{-1}. And high capacitance retention of ~ 69% was observed when the current density was increased to 10 A g^{-1}. Moreover, the Nyquist plots (Fig. 6e) exhibited a linear line parallel to an imaginary axis in the low frequency region together with relatively small values of R_s = 2.9 Ω and R_{ct} = 0.3 Ω. Significantly, as seen in the Ragone plots (Fig. 6f), the supercapacitor delivered a significantly high energy density of 107 Wh kg^{-1} at a power density of 900 W kg^{-1} and retained the remarkable energy density to be 67 Wh kg^{-1} even at a high power density of 18 kW kg^{-1}. These values represent new record ever reported for porous carbons-based supercapacitors (Table 1).

3.5. Origin for the excellent capacitive performance of the 'AHPC'

The excellent capacitive performance of '*AHPC*' can be likely attributed to the natural features of ant. Firstly, the exoskeleton of ant is comprised of chitin, a modified polysaccharide known for the toughness, which could be even superior to the cellulose in plant epidermis as an ideal candidate for the robust 3-D scaffolding frameworks in the carbonation. Consistently, thermo gravimetric curve (Fig. S4) showed the carbonation temperature (*i.e.,* the temperature at which the maximum weight loss was achieved and also carbon skeleton was initially formed) of the ant powder was ~ 400 °C, which is higher than that of the plant biomass (300–350 °C) [43,48,53,54]. Secondly, the ant powder contains various proteins and fatty acids at a high gravimetric weight (up to ~ 60%) [55], which is beneficial for the production of highly porous carbons [31,56]. Moreover, XPS analysis on the *'Control'* sample revealed the presence of elemental carbon, nitrogen, oxygen, and sulfur in the ant powder, whilst EDX indicated the abundance of calcium, magnesium, and manganese. Such unique elemental composition can provide natural templates and heteroatoms instead of the artificial addition of hard templates or chemical substances for the formation of hierarchical porous structure and co-doping.

4. Conclusions

3-D robust framework of hierarchical porous carbons has been derived from ant powder by one-step production. The product exhibits a very large specific surface area of 2650 m^2 g^{-1}, with optimal pore size distributions and good levels of N-O-S heteroatom dopants. These advantageous features have afforded considerably satisfactory energy storage performance, showing a specific capacitance as high as 576 F g^{-1} at a current density of 1.0 A g^{-1} in a three-electrode system, and 352 F g^{-1} at 0.1 A g^{-1} in a two-electrode system, together with a high rate retention (225 F g^{-1} at 20 A g^{-1}) and high cycling stability (only 5% capacitance loss over 10,000 cycles at 10 A g^{-1}). Furthermore, these electrodes have delivered an ultrahigh energy density of 107 Wh kg^{-1} at a power density of 900 W kg^{-1}, and even 67 Wh kg^{-1} at a power density as high as 18,000 W kg^{-1}, among the highest synergetic energy–power outputting properties ever reported for carbon-based supercapacitors. The superior electrochemical properties are closely associated with the unique natural features of ant, including exoskeleton comprised of chitin that facilitates the fabrication of tough 3-D scaffolding frameworks, high proteins and fatty acids composition that forms the highly porous carbons co-doped with heteroatoms, richness of metal salts that provide natural templates for hierarchical porous structure. This work presents the first attempt of using insect biomass for HPCs production. These promising results have introduced a fertile ground by using insect biomass to produce advanced carbons, which may hold considerable potential to be applied in the energy storage industry.

Acknowledgements

This work was financially supported by the National Natural Science Foundation of China (21473045, 51401066, 51772066), and State Key Laboratory of Urban Water Resource and Environment (2018DX04).

Appendix A. Supporting information

Supplementary data associated with this article can be found in the online version at http://dx.doi.org/10.1016/j.nanoen.2018.03.016.

References

[1] Y.G. Wang, Y.Y. Xia, Adv. Mater. 25 (2013) 5336–5342.
[2] H. Jiang, P.S. Lee, C.Z. Li, Energy Environ. Sci. 6 (2012) 41–53.
[3] S.L. Zhang, N. Pan, Adv. Energy Mater. 5 (2015) 1401401.
[4] G.P. Wang, L. Zhang, J.J. Zhang, Chem. Soc. Rev. 41 (2012) 797–828.
[5] Z. Gao, C. Bumgardner, N.N. Song, Y.Y. Zhang, J.J. Li, X.D. Li, Nat. Commun. 7 (2016) 11586.
[6] Y.P. Zhai, Y.Q. Dou, D.Y. Zhao, P.F. Fulvio, R.T. Mayes, S. Dai, Adv. Mater. 23 (2011) 4828–4850.
[7] B. Li, F. Dai, Q.F. Xiao, L. Yang, J.M. Shen, C.M. Zhang, M. Cai, Energy Environ. Sci. 9 (2016) 102–106.
[8] L.L. Liu, Z.Q. Niu, J. Chen, Chem. Soc. Rev. 45 (2016) 4340–4363.
[9] M. Salanne, B. Rotenberg, K. Naoi, K. Kaneko, P.L. Taberna, C.P. Grey, B. Dunn, P. Simon, Nat. Energy 1 (2016) 16070.
[10] F. Xu, Z.W. Tang, S.Q. Huang, L.Y. Chen, Y.R. Liang, W.C. Mai, H. Zhong, R.W. Fu, D.C. Wu, Nat. Commun. 6 (2015) 7221.
[11] H.B. Feng, H. Hu, H.W. Dong, Y. Xiao, Y.J. Cai, B.F. Lei, Y.L. Liu, M.T. Zheng, J. Power Sources 302 (2016) 164–173.
[12] D.H. Zhu, Y.W. Wang, W.J. Lu, H. Zhang, Z.Y. Song, D. Luo, L.H. Gan, M.X. Liu, D.M. Sun, Carbon 111 (2017) 667–674.
[13] Y.X. Xu, Z.Y. Lin, X. Zhong, X.Q. Huang, N.O. Weiss, Y. Huang, X.F. Duan, Nat. Commun. 5 (2014) 4554.
[14] X.B. Wang, Y.J. Zhang, C.Y. Zhi, X. Wang, D.M. Tang, Y.B. Xu, Q.H. Weng, X.F. Jiang, M. Mitome, D. Golberg, Y. Bando, Nat. Commun. 4 (2013) 2905.
[15] J.S. Zhou, J. Lian, L. Hou, J.C. Zhang, H.Y. Gou, M.R. Xia, Y.F. Zhao, T.A. Strobel, L. Tao, F. Gao, Nat. Commun. 6 (2015) 8503.
[16] Y. Liu, Y.T. Shen, L.T. Sun, J.C. Li, C. Liu, W.C. Ren, F. Li, L.B. Gao, J. Chen, F.C. Liu, Y.Y. Sun, N.J. Tang, H.M. Cheng, Y.W. Du, Nat. Commun. 7 (2016) 10921.
[17] T.Q. Lin, I.W. Chen, F.X. Liu, C.Y. Yang, H. Bi, F.F. Xu, F.Q. Huang, Science 350 (2015) 1508–1513.
[18] P. Ghimire, C. Gunathilake, N.P. Wickramaratne, M. Jaroniec, Carbon 121 (2017) 408–417.
[19] J. Yang, H.L. Wu, M. Zhu, W.J. Ren, Y. Lin, H.B. Chen, F. Pan, Nano Energy 33

(2017) 453–461.
[20] X.J. He, X.J. Li, H. Ma, J.F. Han, H. Zhang, C. Yu, N. Xiao, J.S. Qiu, J. Power Sources 340 (2017) 183–191.
[21] S. Dyjak, W. Kiciński, M. Norek, A. Huczko, O. Łabędź, B. Budner, M. Polański, Carbon 96 (2016) 937–946.
[22] J. Zhao, H.W. Lai, Z.Y. Lyu, Y.F. Jiang, K. Xie, X.Z. Wang, Q. Wu, L.J. Yang, Z. Jin, Y.W. Ma, J. Liu, Z. Hu, Adv. Mater. 27 (2015) 3541–3545.
[23] L.T. Qu, Y. Liu, J.B. Baek, L.M. Dai, Acs Nano 4 (2010) 1321–1326.
[24] Y.C. Liu, X.F. Miao, J.H. Fang, X.X. Zhang, S.J. Chen, W. Li, W.D. Feng, Y.Q. Chen, W. Wang, Y.N. Zhang, ACS Appl. Mater. Interfaces 8 (2016) 5251–5260.
[25] H. Peng, J.Z. Zhou, K.J. Sun, G.F. Ma, Z.G. Zhang, E. Feng, Z.Q. Lei, A.C.S. Sustain, Chem. Eng. 5 (2017) 5951–5963.
[26] Y.J. Li, G.L. Wang, T. Wei, Z.J. Fan, P. Yan, Nano Energy 19 (2016) 165–175.
[27] W.J. Qian, F.X. Sun, Y.H. Xu, L.H. Qiu, C.H. Liu, S.D. Wang, F. Yan, Energy Environ. Sci. 7 (2013) 379–386.
[28] Y.F. Zhao, S.F. Huang, M.R. Xia, S. Rehman, S.C. Mu, Z.K. Kou, Z. Zhang, Z.Y. Chen, F.M. Gao, Y.L. Hou, Nano Energy 28 (2016) 346–355.
[29] S.Y. Gao, X.G. Li, L.Y. Li, X.Y. Wei, Nano Energy 33 (2017) 334–342.
[30] C. Chen, D.F. Yu, G.Y. Zhao, B.S. Du, W. Tang, L. Sun, Y. Sun, F. Besenbacher, M. Yu, Nano Energy 27 (2016) 377–389.
[31] Y.S. Yun, S.Y. Cho, J.Y. Shim, B.H. Kim, S.J. Chang, S.J. Baek, Y. Huh, Y.S. Tak, Y.W. Park, S.J. Park, H.J. Jin, Adv. Mater. 25 (2013) 1993–1998.
[32] Y.Q. Zhang, X. Liu, S.L. Wang, L. Li, S.X. Dou, Adv. Energy Mater. 7 (2017) 1700592.
[33] N.N. Guo, M. Li, Y. Wang, X.K. Sun, F. Wang, R. Yang, ACS Appl. Mater. Interfaces 8 (2016) 33626–33634.
[34] X.J. Wei, Y.B. Li, S.Y. Gao, J. Mater. Chem. A 5 (2017) 181–188.
[35] J. Niu, R. Shao, J.J. Liang, M.L. Dou, Z.L. Li, Y.Q. Huang, F. Wang, Nano Energy 36 (2017) 322–330.
[36] X. Yu, Y.B. Kang, H.S. Park, Carbon 101 (2016) 49–56.
[37] A.K. Mondal, K. Kretschmer, Y.F. Zhao, H. Liu, H.B. Fan, G.X. Wang, Micro. Mesopor. Mater. 246 (2017) 72–80.
[38] B. Liu, Y.J. Liu, H.B. Chen, M. Yang, H.M. Li, J. Power Sources 341 (2017) 309–317.
[39] T. Ouyang, K. Cheng, Y.Y. Gao, S.Y. Kong, K. Ye, G.L. Wang, D.X. Cao, J. Mater. Chem. A 4 (2016) 9832–9843.
[40] S.M. Liu, Y.J. Cai, X. Zhao, Y.R. Liang, M.T. Zheng, H. Hu, H.W. Dong, S.P. Jiang, Y.L. Liu, Y. Xiao, J. Power Sources 360 (2017) 373–382.
[41] K. Fic, G. Lota, M. Meller, E. Frackowiaket, Energy Environ. Sci. 5 (2012) 5842–5850.
[42] S.J. Song, F.W. Ma, G. Wu, D. Ma, W.D. Geng, J.F. Wan, J. Mater. Chem. A 35 (2015) 18154–18162.
[43] C.L. Long, X. Chen, L.L. Jiang, L.J. Zhi, Z.J. Fan, Nano Energy 12 (2015) 141–151.
[44] S.Y. Gao, L.Y. Li, K.R. Geng, X.J. Wei, S.X. Zhang, Nano Energy 16 (2015) 408–418.
[45] Y. Zhang, S.S. Liu, X.Y. Zheng, X. Wang, Y. Xu, H.Q. Tang, F.Y. Kang, Q.H. Yang, J.Y. Luo, Adv. Funct. Mater. 27 (2017) 1604687.
[46] Y.J. Cai, Y. Luo, Y. Xiao, X. Zhao, Y.R. Liang, H. Hu, H.W. Dong, L.Y. Sun, Y.L. Liu, M.T. Zheng, ACS Appl. Mater. Interfaces 8 (2016) 33060–33071.
[47] H. Peng, G.F. Ma, K.J. Sun, Z.G. Zhang, Q. Yang, Z.Q. Lei, Electrochim. Acta 190 (2016) 862–871.
[48] E. Raymundo-Piñero, M. Cadek, F. Béguin, Adv. Funct. Mater. 19 (2009) 1032–1039.
[49] B. Duan, X. Gao, X. Yao, Y. Fang, L. Huang, J. Zhou, L.N. Zhang, Nano Energy 27 (2016) 482–491.
[50] Y.Q. Zhao, M. Lu, P.Y. Tao, Y.J. Zhang, X.T. Gong, Z. Yang, G.Q. Zhang, H.L. Li, J. Power Sources 307 (2016) 391–400.
[51] L. Sun, C.G. Tian, M.T. Li, X.Y. Meng, L. Wang, R.H. Wang, J. Yin, H.G. Fu, J. Mater. Chem. A 1 (2013) 6462–6470.
[52] D.W. Wang, S.J. Liu, G.L. Fang, G.H. Geng, J.F. Ma, Electrochim. Acta 216 (2016) 405–411.
[53] G.Y. Xu, J.P. Han, B. Ding, P. Nie, J. Pan, H. Dou, H.S. Li, X.G. Zhang, Green Chem. 17 (2015) 1668–1674.
[54] C. Long, J.L. Zhuang, Y. Xiao, M.T. Zheng, H. Hu, H.W. Dong, B.F. Lei, H.R. Zhang, Y.L. Liu, J. Power Sources 310 (2016) 145–153.
[55] S. Bhulaidok, O. Sihamala, L. Shen, D. Li, Maejo Int. J. Sci. Technol. 4 (2010) 101–112.
[56] C.L. Long, L.L. Jing, X.L. Wu, Y.T. Jiang, D.R. Yang, C.K. Wang, T. Wei, J.L. Zhuang, Carbon 93 (2015) 412–420.